Experimental observations of the main hypothesis employed in the definition of the wTCM finite element under compression

Juan Antonio López-Salido[a], Luis Saucedo-Mora[a]

[a] *E.T.S. de Ingeniería Aeronáutica y del Espacio, Universidad Politécnica de Madrid, Pza. Cardenal Cisneros 3, 28040, Madrid, Spain*

Abstract

Auxetic metamaterials, characterized by their negative Poisson's ratio, offer unique mechanical properties such as enhanced energy absorption, improved indentation resistance, and high shear stiffness, making them promising candidates for advanced engineering applications. This work presents experimental and numerical analyses of a 3D-printed coupon based on the General Auxetic Metamaterial (GAM) cell. A quasi-static compression test was performed to validate the auxetic behavior and to characterize the deformation and failure mechanisms. In parallel, an innovative multiscale finite element methodology based on the wTCM element was applied to replicate the mechanical response of the structure with significantly reduced computational cost. The results demonstrate strong agreement between experimental observations and numerical predictions in terms of global auxetic response, axial force-displacement behavior, and local failure modes. Once properly calibrated, the methodology enables accurate prediction of volumes with different sizes and geometries, thereby reducing the need for extensive experimental campaigns and enabling the efficient simulation of large-scale metamaterial structures.

Keywords: wTCM, metamaterial, experimental test, FEM calculation, multi-sacale

1. Introduction

Auxetic metamaterials (engineered architectures with a negative Poisson's ratio) exhibit the counterintuitive behavior of lateral expansion under axial compression or elongation under tension [11]. Their unique deformation mechanism enhance the energy absorption, gives excellent indentation and fracture resistance, and high shear stiffness qualities supported by extensive theoretical and experimental studies [5]. In fields such as aerospace, biomechanics, protective systems, or soft robotics, these advantageous properties position makes auxetics extremely promising candidates for future structures engineering [7].

Recent research has explored diverse auxetic architectures—including re-entrant honeycombs, chiral lattices, rotating rigid units, and origami-inspired designs—through advanced simulation and manufacturing techniques [10]. Specific structural designs like REC configurations have demonstrated notable gains in energy absorption via combining Finite Element analyses and physical testing [4].

Despite these advances, FEM-based simulations alone cannot fully capture real-world behavior of auxetic structures. Manufacturing defects, material heterogeneity, boundary conditions, and geometric imperfections or simply very complex geometries often lead to significant deviations between simulated and actual performance or simply make the FEM simulation unaffordable. Hybrid experimental-simulation approaches are vital: they

enable validation and calibration of FEM models—improving predictive accuracy—and provide deeper insight into deformation mechanisms and failure modes under actual loading.

In this study, a compression test on a 3D-printed auxetic metamaterial coupon structure is conducted, complemented by several simulation models that will capture the nonlinear behaviour of the structure. A detaile FEM model will be developed to obtain the geometric nonlinearities of the coupon and an innovative methodology for multiscale FEM simulations applied on metamaterial structures will be developed to capture both geometric and material nonlinearities. The main goals is to: (1) validate the negative Poisson's ratio behaviour of the metamaterial structure, checking its mechanical response, and failure behavior; (2) validate an innovative methodology to fastly simulate metamaterial structures with quantitatively accurate results; (3) elucidate deformation mechanisms and energy absorption phenomena driving auxetic performance under compression. This integrated procedure strengthens proposed-FEM robustness and advances the application potential of auxetic metamaterials in real-world engineering.

2. Methodology

This section provides a detailed analysis of both the experimental procedures and the numerical simulations. First, it presents a comprehensive description of the manufactured coupon, covering the manufacturing process and the development of the experimental testing campaign. In parallel, the same test is analyzed through finite element (FE) simulation models. A detailed FE model with large displacement capabilities (including geometric nonlinearity) is developed to investigate the nonlinear response of the structure. In addition, the simulation is complemented by the formulation and development of an equivalent multiscale FEM model, designed to efficiently reproduce the behavior of metamaterial structures while capturing key nonlinearities such as buckling (geometric) and damage (material). A detailed description of the manufactured coupon, a brief overview of the testing equipment, and a summary of the simulation models employed are now exposed.

2.1. Coupon model geometry. 3D printing.

The proposed structure to be tested is based on the GAM (General Auxetic Metamaterial) cell [3, 12]. This cell has the particularity of developing different behaviors depending on the connectivity of the different metamaterial layers. For this case, auxetic configuration is chosen, and cell parameters are exposed on the following table:

GAM Cell (Unit Dimensionless Cell)									
$\mathbf{v_1}$	$\mathbf{v_2}$	$\mathbf{Step_x}$	$\mathbf{Step_y}$	$\mathbf{H_{star}}$	$\mathbf{D_{star}}$	$\mathbf{H_{prism}}$	$\mathbf{R_{bars}}$ **[mm]**	**N. Cells**	**Scale Factor**
-0.4	0.2	1	1	0.25	0.3	1.6	1.0	In Layer: 19 ; Layers: 7	17.5

Table 1: Auxetic and non auxetic cell structure parameters.

Based on these parameters, a hexagonal-based metamaterial structure is generated and extruded, composed by 133 metamaterial cells. This configuration defines the coupon that will be manufactured, which is shown below:

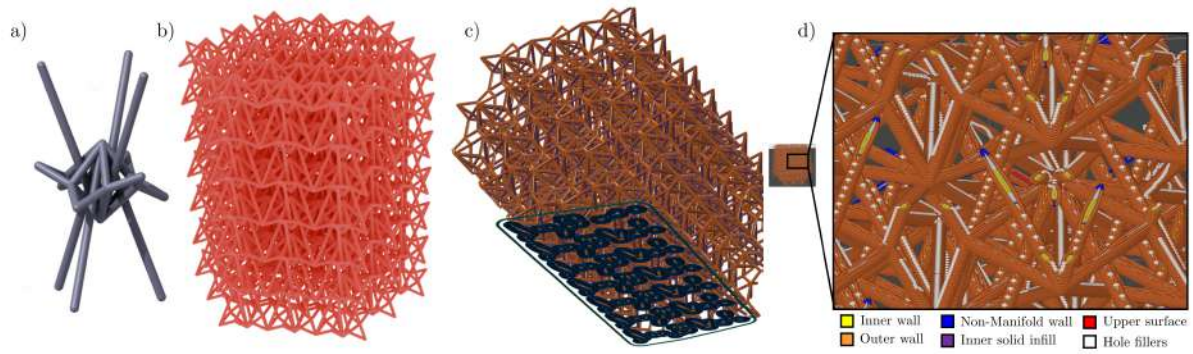

Figure 1: Metamaterial coupon. a) GAM cell geometry. b) Coupon geometry. c) Coupon manufacturing layout. d) Coupon geometry slicing strategy.

The coupon was produced using fused deposition modelling (FDM) technology and a Bambu Lab X1-Carbon printer [1]. This printer is equipped with a high-precision extrusion system with a hardened metal hotend, a 0.2 mm hardened steel nozzle, and hardened steel extruder gears. The extruder can reach a maximum temperature of 300 °C, while the hot bed can operate up to 110 °C (at 220 V). The available manufacturing volume is 256 x 256 x 256 mm^3.

In terms of performance, the printer supports print speeds of up to 500 mm/s and has a maximum acceleration of 20 m/s^2. It features closed control fans for cooling the hotend, the piece and the compartment to ensure optimal printing. The automatic bed levelling system ensures proper filament adhesion throughout the printing process.

The material used was PLA Bambu Basic, a polylactic acid designed for high-speed printing [2]. The filament has a nominal diameter of 1.75 mm and is supplied on 1 kg spools. The mechanical properties of this PLA used are summarised in the table below:

Table 2: Mechanical and thermal properties of Bambu Basic PLA in X-Y plane and Z direction.

Direction	E $[GPa]$	σ_{UTS} $[MPa]$	ε_{UTS} [%]	ρ $[kg/m^3]$	T_m $[^oC]$
X-Y	2.58 ± 0.22	35 ± 4	12.2 ± 1.8	1240	160
Z	2.06 ± 0.17	31 ± 3	7.5 ± 1.3		

2.2. Experimental set up.

The compression test was performed using a Servosis servohydraulic frame equipped with an Instron 8800 actuator of 250 kN capacity [13, 6]. Force was measured with a 100 kN Instron load cell. The experimental setup included a double-column frame with a top-mounted hydraulic actuator, and a closed-loop electronic control system for force and displacement.

The coupons were fixed by means of two flat compression plates, one upper and one lower. This arrangement enables a uniform compression load to be applied, thereby minimising the effects of slippage or misalignment. The plates are coaxially aligned and adapted to rigidly clamp 3D-printed samples.

The test was carried out at a speed of 1 mm/min to ensure quasi-static conditions during the deformation of the structure. This low speed minimises dynamic effects and ensures a controlled load application, which is essential for an accurate analysis of the overall mechanical behaviour of the PLA metamaterial specimen.

The system also features a digital control console, real-time monitoring and an emergency stop button. Images of both machine and test set up are shown below:

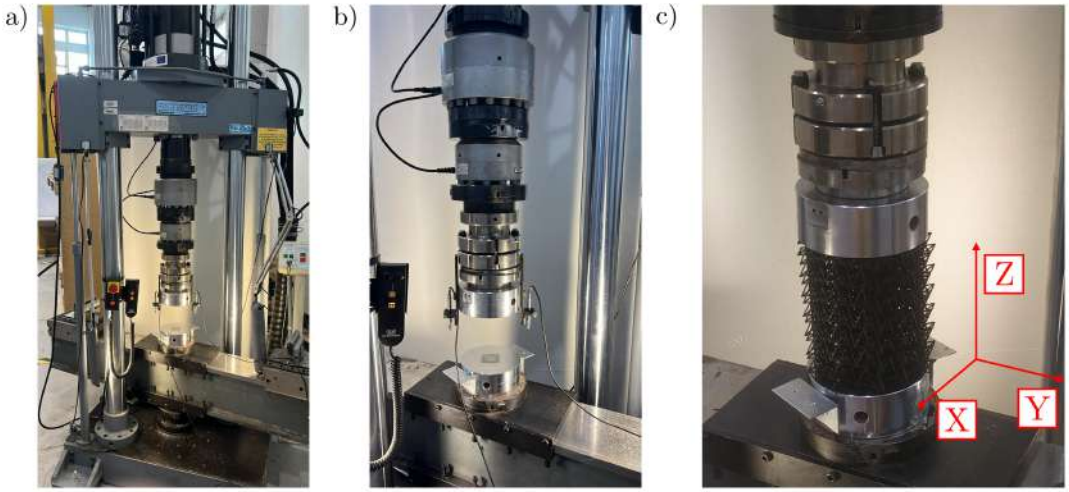

Figure 2: Tensile bench test layout. a) General view. b) Tie plate area view. c) Coupon positioned at tie plates.

2.3. Geometrical nonlinearity. Explicit FEM.

In order to rigorously validate the FEM methodology developed in the following section, an explicit finite element (FE) model is first developed (a strategy commonly employed in the analysis of metamaterial structures). This model was implemented using FEBio, an open-source finite element software primarily designed for biomechanical applications, but widely adopted for solving complex solid mechanics problems involving large displacements and geometric nonlinearities [9]. FEBio enables the explicit simulation of highly nonlinear problems, making it particularly suitable for modeling structures with complex geometries, such as metamaterials, whose behavior is strongly influenced by local buckling of the struts.

In the present study, a static loading scenario is simulated by gradually imposing compressive displacements while recording the corresponding load response at the reaction points throughout the process. The analysis explicitly accounts for large displacements, allowing accurate capture of geometric nonlinear effects, such as local buckling, and providing a high-fidelity representation of the structural response. The material model employed is isotropic (neo-Hookean), with a Young's modulus equal to half of the value reported in Table 2. This reduction is attributed to inherent defects from the manufacturing process, as well as the effect of print directionality on the final material properties. The finalized material parameters are summarized in Table 3.

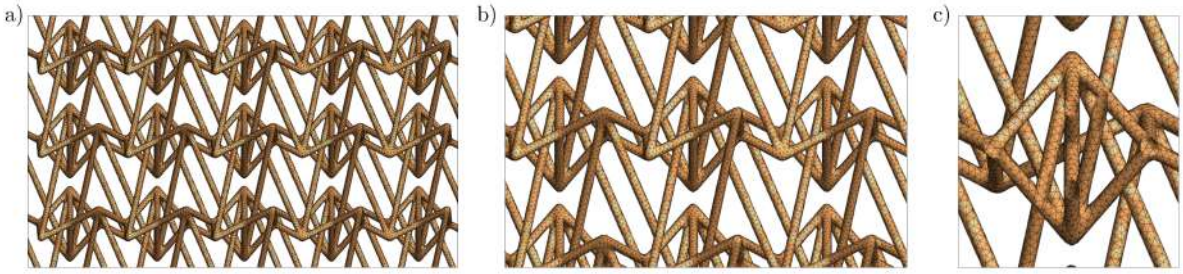

Figure 3: Detailed explicit FEM mesh: a) Through-layers mesh view. b) Cells mesh in a single layer view c) Cell mesh detailed view.

The initial geometry for the development of this model is similar to that shown in Fig. 1b). Due to the high geometric complexity of the coupon, a large number of finite elements is required, and the only feasible meshing strategy is the use of tetrahedral elements. To reduce computational cost, a single-point integration scheme has been adopted, significantly decreasing simulation time. No contact interactions are implemented in the FE model. The generated mesh provides sufficient resolution in critical regions, enabling accurate capture of the nonlinear phenomena associated with the complex geometry of the metamaterial. A summarizing table for this case is exposed below:

Table 3: Configuration parameters for explicit finite element model.

$E\ [GPa]$	ν	Mat. Model	Contacts	Non Lin.	N. Nodes	N. Elements
0.9888	0.3	isotr. neo-Hookean	No	Geometric	481 888	1 351 050

This explicit FE approach, together with the experimental campaign, serves as a benchmark for assessing the performance and accuracy of the subsequent multiscale FEM methodology, particularly in reproducing nonlinear phenomena such as buckling and material damage in metamaterial architectures.

2.4. Geometrical and material nonlinearities. Implicit wTCM FEM methodology.

An innovative methodology is proposed for the development of simulation models capable of cuantitatively predict the behavior of metamaterial structures with significantly reduced computational cost, in line with the approach presented by López-Salido and Saucedo-Mora [8]. Firstly, the geometry of the metamaterial to be manufactured has been developed using pentahedral elements. In this case, once the internal arrangement of the struts within the elements is defined, it is replicated in space and connected to form the geometry shown in Figure 1.

In parallel, a FEM model has been developed using pentahedral elements in which the effect of the internal struts is retained. This effect is considered by accounting for their local configuration and deformation at each calculation step. The element properties (specifically, the Young's modulus) are dynamically updated to accurately capture the equivalent behavior of the metamaterial structure.

The inputs required for the FEM model are an initial value of Young's modulus (E_0), which is updated dynamically during the first iteration until convergence is achieved, thus having little influence on the final result. However, the Poisson's ratio is constant and must be defined for the entire simulation. In this case, a Poisson's ratio of -0.5 was selected based on the deformation observed in the experiment, which closely matches the value derived from comparing the axial and cross deformations observed in it. The measurement of the Poisson's ratio is described in the Results section.

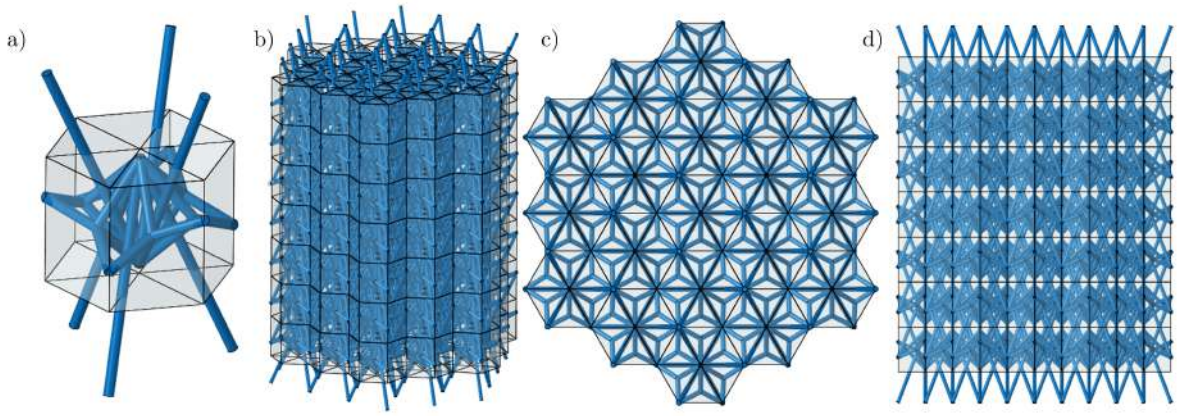

Figure 4: Metamaterial structure generated from pentaheral element. a) Cell equivalence. b) Coupon equivalence, iso view. c) Coupon equivalence, top view. d) Coupon geometry, front view.

As shown in Figure 4, the patterned structure within a single unit cell is replicated to generate the target coupon model. Within this methodology, calibration curves are employed for the different struts composing the unit cell. These curves capture the behavior of the struts across different regimes, including the linear elastic region and the nonlinear regions, where various effects such as geometric buckling and material damage become significant.

2.4.1. Implicit wTCM FEM Methodology with Geometric Nonlinearities

The proposed methodology allows for the retention of all nonlinear effects through the calibration curves assigned to the struts within the element. By using the curves developed in the previous section, it is possible to reproduce all the nonlinear phenomena observed during experimentation. For comparison with the explicit model, it is only necessary to adjust the calibration curves to retain geometric nonlinearity while excluding material nonlinearity, which is associated with stiffness degradation. Mesh model will be the same, so computational cost will be similar.

3. Results.

This section analyzes the results obtained for the three proposed approaches. First, the linear region of the explicit model and the experimental results are directly compared with the innovative methodology proposed. Subsequently, the global structural response is examined for the different cases, and local effects observed during compression are analyzed for all approaches, assessing their validity and similarity.

3.1. Linear behaviour validation.

This section presents the results obtained from the experimental test, the explicit FE approach and the simulation using the wTCM element [8]. The primary aim is to demonstrate how an appropriate calibration of the proposed simulation methodology enables the quantitative prediction of the metamaterial's behaviour under specific loading conditions. First, Digital Image Correlation measurement of the experimental test is compared with the results obtained through FEM, at the moment when the test reaches an axial compression of 3 mm.

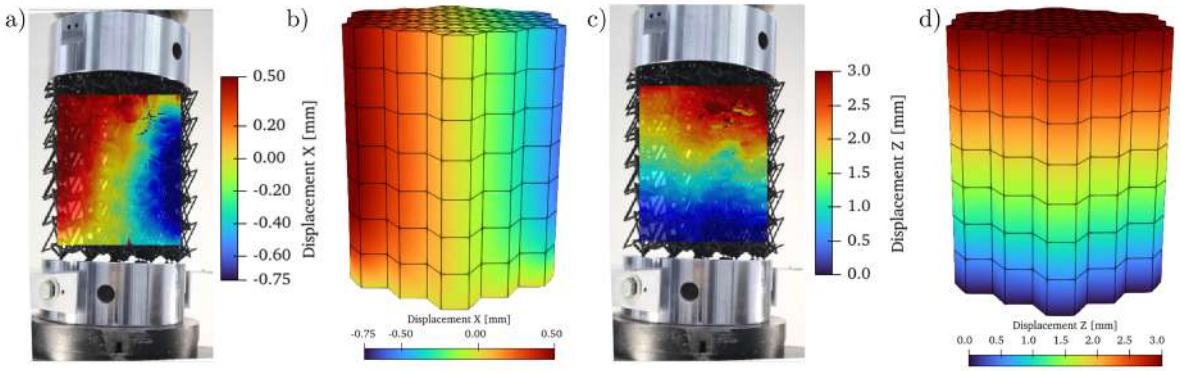

Figure 5: Displacement field for the test and the simulation at an intermediate load step. a) Test cross displacement. b) wTCM FEM cross displacement (buclking and damage nonlin.). c) Test axial displacement. d) wTCM FEM axial displacement (buckling and damage nonlin.).

At this stage, it can be observed that both the experiment and the simulation quantitatively record the same state of axial displacements, and a very similar state of cross displacements. In the x displacement of Figure 5a there is a small misalligment that can be given by a small out-of-plane movement of the sample, or a small anisotropy of the metamaterial. With those measurements, and considering the size of the sample, a Poisson's ratio of -0.5 is calculated. This demonstrates that the proposed methodology provides an accurate approach to the real behavior of the structure and that the structure has a negative Poisson's ratio.

Additionally, the same displacement state in the linear regime of the explicit FE model is analyzed and compared with the model developed using the wTCM methodology.

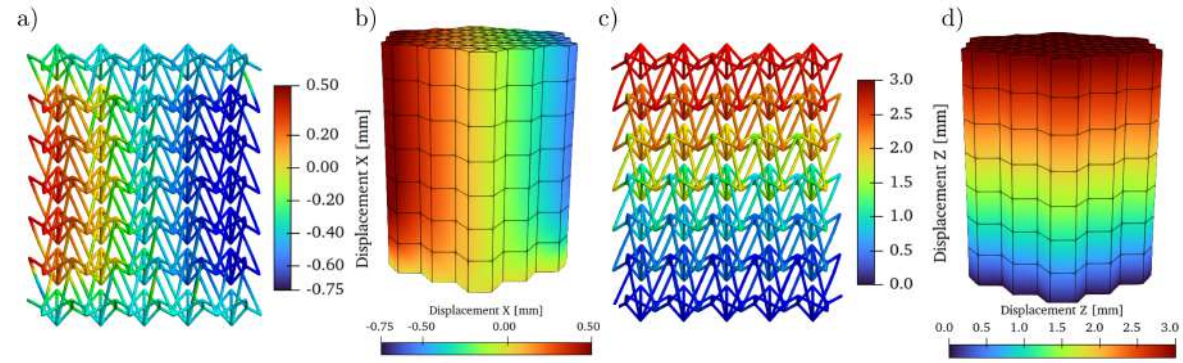

Figure 6: Displacement field for the detailed explicit FE simulation and wTCM simulation at an intermediate load step. a) Explicit FE cross displacement. b) wTCM FEM cross displacement (buckling nonlin.). c) Explicit FE axial displacement. d) wTCM FEM axial displacement (buckling nonlin.).

Based on the results of the comparison, several important conclusions can be drawn. First, a clear quantitative correlation in displacements is confirmed for both models. The axial and crossed displacement fields are highly similar in both cases. Furthermore, in the explicit model no anisotropy as the one found at image digitization process is present, resulting in a homogeneous and continuous displacement distribution across the structure for both approaches.

On the other hand, when analyzing the results obtained with the wTCM model containing geometric nonlinearity, it is observed that both the displacement values and their distribution are equal to those of the explicit FE model that includes damage effects

(hereafter referred to as the both buckling and damage-inclusive model). This outcome can be explained by the fact that, although the two models account for different types of nonlinear behavior in the nonlinear regime, their response in the linear regime is essentially the same. Consequently, the displacement maps remain consistent across the different wTCM models.

3.2. Global behaviour validation.

This section analyzes the global behavior of the structure across the three approaches. First, the calibration curves employed in the wTCM models are examined in detail (Fig. 7a). The solid lines correspond to the model that includes both geometric and material nonlinearities (G&M), while the dashed lines represent the model accounting just for geometric nonlinearity (G). As anticipated, these curves are identical in the linear regime; however, their responses diverge in the nonlinear regime, where the distinct effects of each nonlinearity behaviour become evident.

Furthermore, Fig. 7b presents the force-displacement curves under compression for the three approaches.

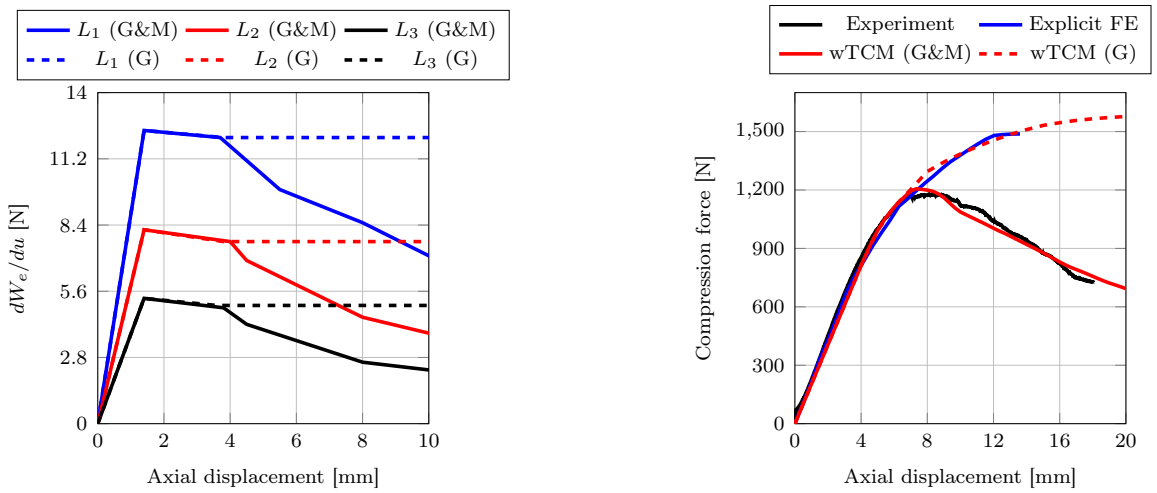

a) b)

Figure 7: a) FEM calibration curves for axial compression with the wTCM element. $L_1 = 10.79mm$, $L_2 = 14.93mm$, $L_3 = 43.54mm$. Solid lines for geometric and material nonlinearities, dashed lines for just geometric nonlinearities. b) Axial compression force-displacement curves for all the approaches.

Based on the results exposed, the following conclusions can be drawn:

- The calibration curves are consistent. The curves for both wTCM models are identical in the linear regions. Their divergence in the non-linear regime reflects the stiffness loss of the struts in the damage-included model, which is coherent with the phenomena captured.

- The results are consistent in the linear regime. The force-displacement curves obtained from the experiment, the explicit FE model and the wTCM-based models all show a clear and direct correlation in this region.

- The wTCM methodology proves to be versatile, and its validity is reaffirmed. The model that incorporates both damage and buckling effects successfully reproduces the experimental observations. Similarly, the model that considers only buckling fits

well with the explicit FE model curve, which considers only geometric nonlinearity. These outcomes strengthen the robustness and validity of the proposed methodology.

Thus, the correlation among the three approaches for the global behavior of the structure is confirmed.

3.3. Expermiental local effects.

During the experimental campaign, several local effects were identified. Some of these effects arise from the complex geometry of the metamaterial structure itself, while others are inherent to the manufacturing process of the coupon. These effects are analyzed in detail below, with reference to Fig. 8:

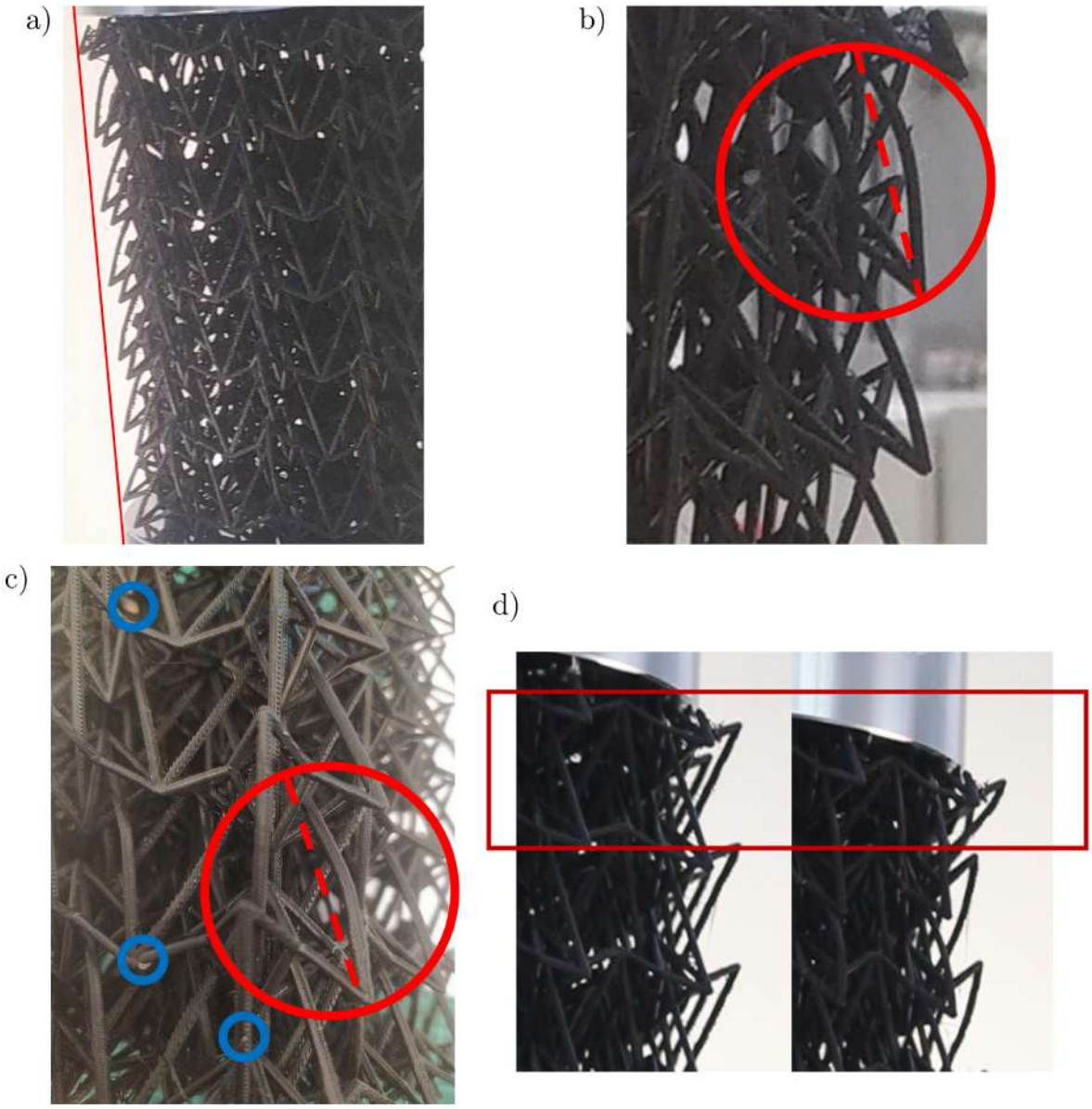

Figure 8: Auxetism effect on GAM structure along the compression test. a) Global auxetic effect at a specific step on compression test; b) Detailed view of the failure of the longest bars while the compression test is carried out; c) In red: remaining plastic strain deformation in GAM structure after unloading. In blue: local failure found at strut joints. d) Local failure of the first layer at final states of the compression loading.

As anticipated in Figure 5a, the global auxetic behaviour of the structure during compression is clearly visible, and is also highlighted in Figure 8a. The onset of the nonlinear regime is evident when nonlinear phenomena, such as buckling of the slenderest struts, appear during the loading process, as shown in Figure 5b. Figure 5c illustrates material nonlinearities through the failure modes observed after unloading the structure, including breakage at certain joints and visible plastic deformation at other connections. Similarly, permanent deformation was observed in the longest struts, which remain deformed once the structure is unloaded.

Finally, Figure 5d clearly shows the local failure of the first layer of the auxetic metamaterial, which is caused by the buckling and subsequent fracturing of the vertical connectivity struts. This type of localised failure is particularly relevant from a simulation perspective.Although it is highly localised, it has a strong impact on the global structural collapse.

Overall, these local phenomena will be compared in detail with those observed in the simulation models, which are analyzed in depth in the following section.

3.4. Simulation local effects.

Finally, the local effects are analyzed from the simulation perspective. As demonstrated in the previous section, the first nonlinear phenomenon to appear is buckling, which is accurately captured by the explicit FE model. This is particularly important because the onset of buckling in slender struts largely governs the subsequent structural response and failure mechanisms. The following figure provides a detailed visualization of these effects on the explicit FE:

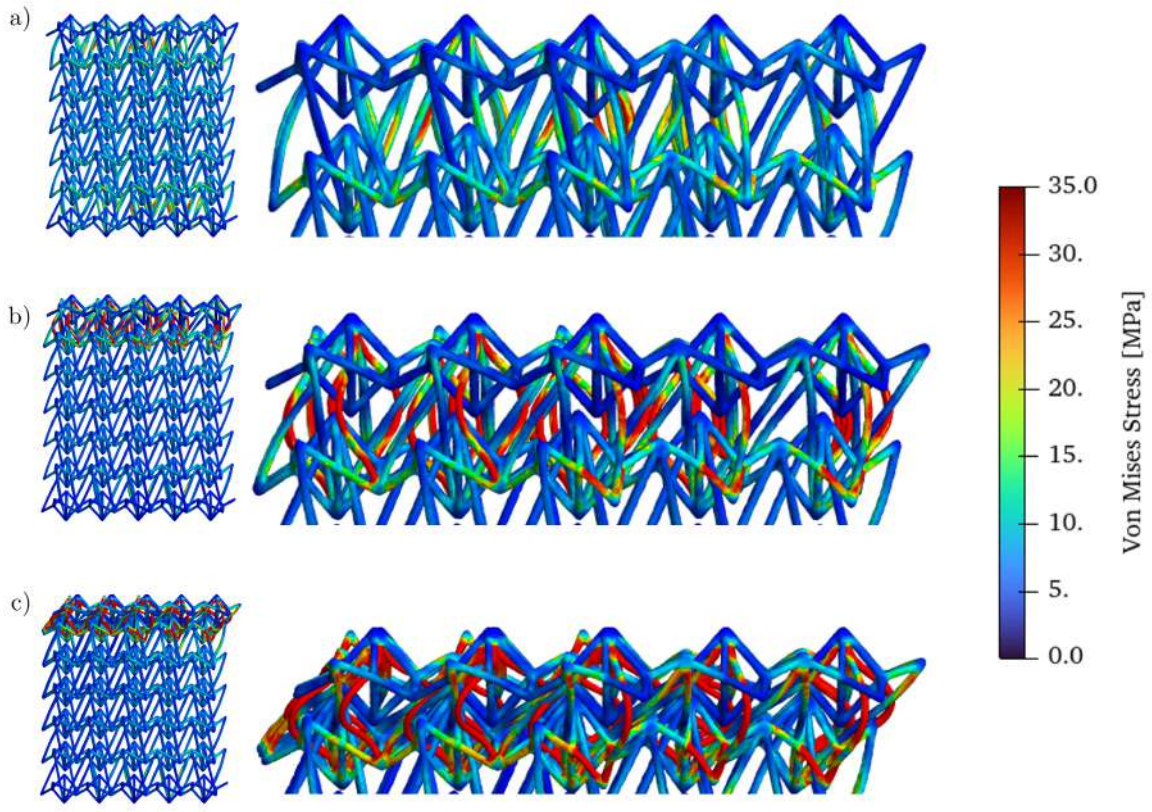

Figure 9: Local failure of first layer found on explicit FE model. a) Beggining of buckling phenomenon. b) Evolution of buckling phenomenon along compression process. c) Final state of local failure of first layer due to buckling phenomenon.

As shown in Figure 9a, geometric nonlinearity induces local buckling of the slenderest struts in the explicit FE model. This phenomenon can also be examined in greater detail in Figure 11b), where the localized buckling of these struts is clearly illustrated. Notably, this response closely matches the experimental observations reported in Figures 8b) and c), confirming the ability of the explicit model to accurately capture the onset and progression of local instabilities that dominate the structural behavior. Moreover, the failure of these struts is localized in the first layer, (named as the boundary layer), which coincides with the local failure observed experimentally. This phenomenon is also detected by the wTCM model, where a change in stiffness is observed in the axial force-displacement curve corresponding to the onset of buckling. However, the stiffness continues to increase monotonically in the explicit model and the subsequent wTCM model, as no plasticity model has been implemented for this case.

Figures 9b) and c) illustrate the development of this buckling behavior without considering strut failure. It is important to note that, while the small in-plane sliding observed in the last figure appears to be captured experimentally, its magnitude is very limited. Before this state could fully develop, other phenomena would occur, such as inter-layer contact or strut fracture due to exceeding the ultimate tensile stress. This highlights that certain localized effects observed in the simulation may be partially constrained or suppressed in the real structure by additional failure mechanisms not explicitly modeled in the FE simulations. Figure 10 provides a detailed analysis of this phenomenon too, emphasizing its relevance as it anticipates through simulation the local effect that is later observed experimentally:

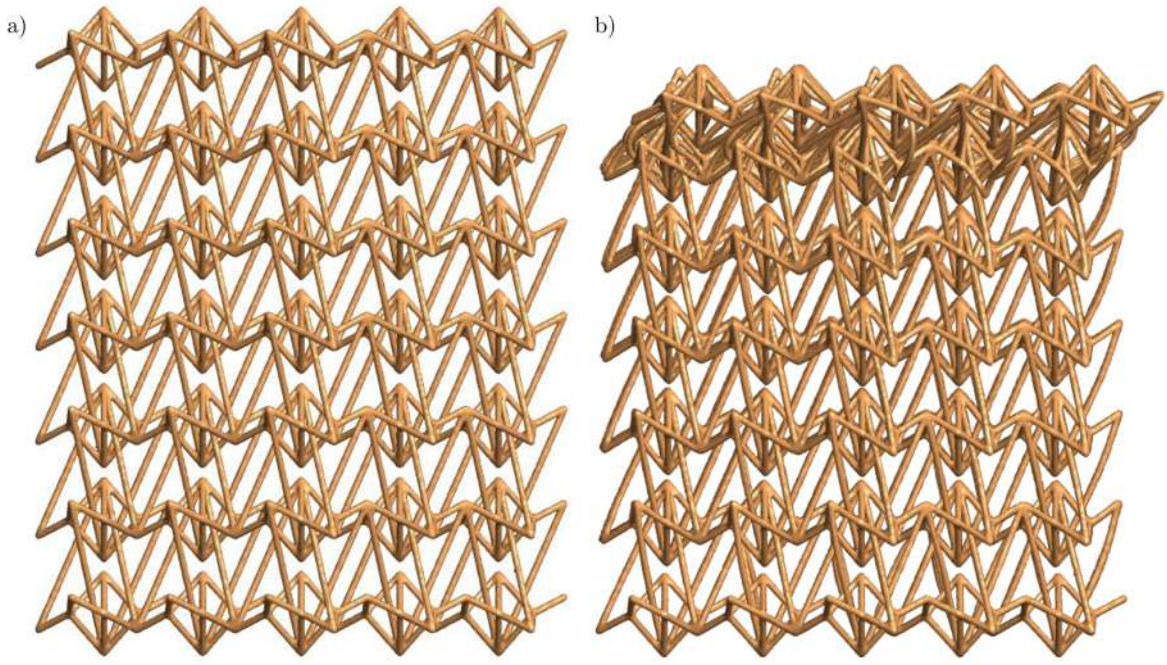

Figure 10: Explicit FE mesh. a) before compressing. b) after compression, where failure at boundary layer has been developed.

On the other hand, carefully analysing the model using the wTCM methodology, local effect can be found too. Specifically, this is analysed in the following image.

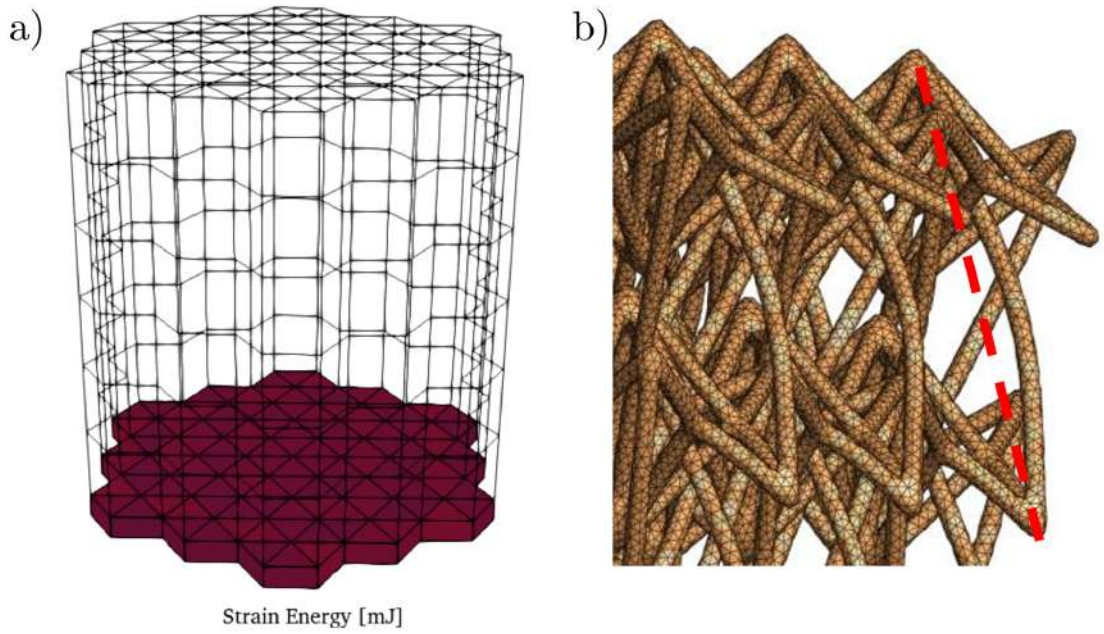

Figure 11: Isolated limit layer failure for the axial compression test: a) Captured phemonemon at the multi-scale FEM, filtered with a strain energy criterion of >50 mJ. b) Local buckling of slenderest bars at explicit FE model.

As can be observed, the wTCM model shows a concentration of strain energy in the elements of the boundary layer, clearly highlighting the local failure of the structure in this layer in a much faster and more straightforward manner than the explicit model. As expected, this local effect, observed during the experimental campaign, is successfully captured by the proposed methodology.

This demonstrates the robustness of the approach, which employs an equivalent FEM model with TCM elements that can be pre-calibrated to accurately predict the behavior of auxetic metamaterial structures. Moreover, the methodology allows for the consideration of several nonlinear phenomena, ranging from geometric buckling to moderate material plasticity, as discussed throughout this article.

3.5. Discussion of problem complexity reduction

Finally, the impact of implementing this methodology on computational performance is analyzed. It is evident that it leads to a significant reduction in resource requirements, as the number of degrees of freedom is drastically reduced. One of the key advantages of the wTCM element methodology lies in the fact that the mesh used across the different models remains unchanged, with no need for further refinement. All the relevant information is embedded in the calibration curves, which govern the behavior of the struts. Consequently, the computational cost is not affected by how these curves evolve to retain different nonlinear responses. This feature makes the approach particularly efficient, as it decouples mesh complexity from material and geometric nonlinearities, allowing the methodology to handle diverse structural behaviors without additional meshing effort. This point can be checked in next figure:

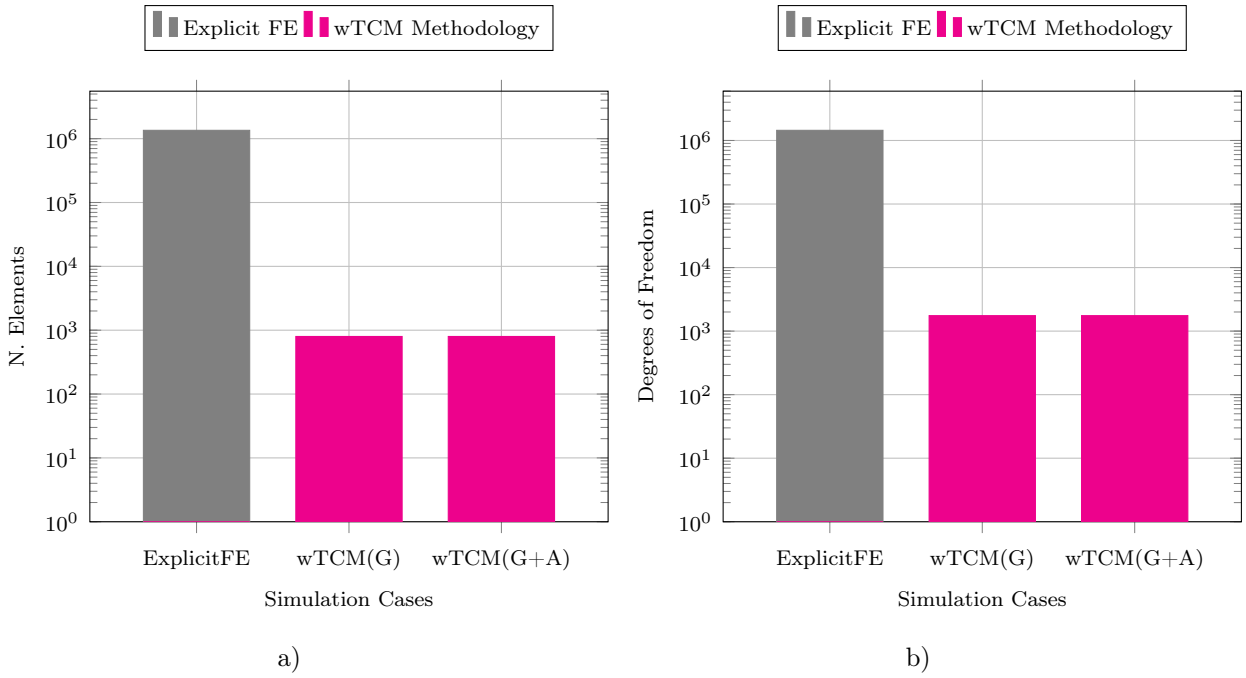

Figure 12: a) Bar chart comparing the number of elements across the three approaches. b) Bar chart comparing the number of degrees of freedom (DOFs) across the three approaches.

As illustrated in figure 12, a gain of three orders of magnitude is achieved both in the number of elements and in the total degrees of freedom. Furthermore, as previously demonstrated in [8], the main potential of the methodology lies in the ability to perform a simple pre-calibration on reduced models, which then allows the reliable prediction of the behavior of mesoscale models with high confidence. This capability makes the methodology not only efficient but also scalable to larger and more complex structures.

By establishing an equivalence between the struts and pentahedral elements, the methodology enables simulations to be carried out with significantly reduced computational time and moderate hardware requirements. This represents a major advantage over other modeling approaches, such as beam-element models or detailed tetrahedral-element models, which may involve hundreds of thousands of degrees of freedom. Remarkably, the complete simulation was executed in just 33 minutes on a computer with 16 GB of RAM and an 8-core processor, implemented in MATLAB using a serial code.

4. Conclusions

After the development of all sections, it can be concluded that both the explicit model and the wTCM models adequately correlate with the phenomena observed in the experiment, while accounting for the specific effects captured by each model. On one hand, the explicit FE model accurately captures the geometric nonlinearity, which is the first to manifest when slender bars begin to buckle. This phenomenon aligns with experimental observations and is similarly to the one captured by the wTCM model, which accounts for the loss of stiffness. However, the explicit model diverges from the experimental results when material nonlinearity becomes significant (plasticity and failure).

At this point, the model developed using the wTCM methodology becomes particularly relevant, as it demonstrates its strength. Once properly calibrated for a single case, the proposed methodology can predict the behavior of volumes of different sizes and geometries. Furthermore, it retains the ability to capture multiple nonlinearities, such

as geometric and material effects, without imposing a higher computational cost. This capability significantly reduces the number of experimental tests required to characterize the response of metamaterial structures, leading to substantial savings in both cost and time.

Moreover, the methodology allows for the numerical simulation of large metamaterial volumes at an affordable computational cost, making it feasible to analyze large-scale structures from a simulation standpoint. Finally, it is important to emphasize that the simulation models capture the local effects that emerge during experimentation with considerable accuracy and detail, enhancing their validity and robustness.

Acknowledgements

The authors would like to express their sincere gratitude to the Department of Applied Mechanics and Project Engineering of the School of Civil Engineering (ETSI Caminos, Canales y Puertos) at the University of Castilla-La Mancha for their support and assistance during the development of this research.

References

[1] Bambu Lab. *Bambu Lab X1-Carbon Technical Specifications*. Bambu Lab, June 2024. Retrieved from internal documentation.

[2] Bambu Lab. *Bambu PLA Basic Technical Data Sheet*. Bambu Lab, June 2024. Version 3.0. Retrieved from internal documentation.

[3] Ismael Ben-Yelun, Guillermo Carano, Francisco Millán, Miguel Gomez, Francisco Leal, and Luis Saucedo Mora. The gam (general auxetic metamaterial): A tuneable internal structural configuration to change the auxetic response with the same unit cell boundary geometry. *SSRN Electronic Journal*, 2022.

[4] Ehsan Etemadi, Mahbubeh Hosseinabadi, Mohsen Taghizadeh, Fabrizio Scarpa, and Hong Hu. Enhancing the energy absorption capability of auxetic metamaterials through auxetic cells within re-entrant circular units. *Engineering Structures*, 315:118379, 2024.

[5] Dong Han, Xin Ren, Yi Zhang, Xiangyu Zhang, Xuegang Zhang, Chen Luo, and Yi Xie. Lightweight auxetic metamaterials: Design and characteristic study. *Composite Structures*, 293:115706, 2022.

[6] Instron Corporation. *Instron 2580 Series Static Load Cells Data Sheet*, 2024. Accessed: 2025-08-26.

[7] Vladislav A Lvov et al. Auxetic metamaterials for biomedical devices: Current situation, main challenges, and research trends. *Materials*, 15:1439, 2022.

[8] Juan Antonio López-Salido and Luis Saucedo-Mora. The wedge topologically consistent metamaterial element (wtcm) for the generation of auxetic metamaterials in complex components and its multi-scale numerical calculation with small geometrical and material non-linearities. *Finite Elements in Analysis and Design*, 252:104456, 2025.

[9] Steve A Maas, Benjamin J Ellis, Gerard A Ateshian, and Jeffrey A Weiss. Febio: Finite elements for biomechanics. *Journal of Biomechanical Engineering*, 134(1):011005, 2012.

[10] T. Meier, R. Li, S. Mavrikos, and X. Jiang. Obtaining auxetic and isotropic metamaterials in counterintuitive design spaces: an automated optimization approach and experimental characterization. *npj Computational Materials*, 10, 2024.

[11] Xin Ren, Raj Das, Phuong Tran, Tuan Ngo, and Yi Xie. Auxetic metamaterials and structures: a review. *Smart Materials and Structures*, 27, 2018.

[12] Luis Saucedo Mora, Guillermo Gómez Carano, Miguel Ángel Sanz Gómez, and Francisco Javier Montáns Leal. Método para modificar la respuesta auxética de una celda sin cambiar su geometría. Technical Report ES2907514B2, Oficina Española de Patentes y Marcas, 2022. `https://consultas2.oepm.es/pdf/ES/0000/000/02/90/75/ES-2907514_B2.pdf`.

[13] Servosis S.A. *General Catalogue of Servo-Hydraulic Testing Machines EFH/300 kN*. Servosis S.A., 2021. Hydrostatic bearing actuator, dual-piston system, load capacity 250–300 kN.